

# Gravitational Lensing of Distant Supernovae

P. Premadi

*Bandung Institute of Technology, Bandung, Indonesia*

H. Martel

*Université Laval, Québec, Qc, G1K 7P4, Canada*

We use a series of ray-tracing experiments to determine the magnification distribution of high-redshift sources by gravitational lensing. We determine empirically the relation between magnification and redshift, for various cosmological models. We then use this relation to estimate the effect of lensing on the determination of the cosmological parameters from observations of high- $z$  supernovae. We found that, for supernovae at redshifts  $z < 1.8$ , the effect of lensing is negligible compared to the intrinsic uncertainty in the measurements. Using mock data in the range  $1.8 < z < 8$ , we show that the effect of lensing can become significant. Hence, if a population of very-high- $z$  supernovae was ever discovered, it would be crucial to fully understand the effect of lensing, before these SNe could be used to constrain cosmological models.

## 1. INTRODUCTION

High-redshift supernovae have become a major tool in modern cosmology. By measuring their apparent magnitudes, we can estimate their luminosity distances  $d_L$  (see [1, 9, 10], and references therein). Since the relationship between  $d_L$  and the redshift  $z$  depends on the cosmological parameters, observations of distant SNe can constrain the cosmological model. Prior to the announcement of the WMAP results [2], observations of high- $z$  SNe provided the most compelling evidence of the existence of a nonzero cosmological constant.

The luminosity distances  $d_L$  are determined by combining the observed fluxes  $F$  with estimates of the SNe luminosities  $L$ . Uncertainties in  $d_L$  are caused by uncertainties in  $L$ , because SNe are not perfect standard candles. The flux  $F$  is much easier to measure, but for distant sources the value of  $F$  might be altered by gravitational lensing caused by the intervening distribution of matter. For instance, a positive magnification would result in an increase in  $F$ , and an underestimation of  $d_L$ .

## 2. THE ALGORITHM

We have developed a *multiple lens-plane algorithm* to study light propagation in inhomogeneous universes [5, 6, 7, 8]. In this algorithm, the space between the observer and the sources is divided into a series of cubic boxes of comoving size 128 Mpc, and the matter content of each box is projected onto a plane normal to the line of sight. The trajectories of light rays are then computed by adding successively the deflections caused by each plane.

To use this algorithm, we need to provide a description of the matter distribution along the line of sight. Matter is divided into two components: background matter and galaxies. We use a P<sup>3</sup>M algorithm to simulate the distribution of background matter. The sim-

ulations used  $64^3$  equal-mass particles and a  $128^3$  PM grid, inside a comoving volume of size 128 Mpc. The matter distribution in the different cubes along the line of sight then corresponds to the state of the simulation at different redshifts.<sup>1</sup> We then use a Monte Carlo method for locating galaxies into the computational volume [4, 6]. Galaxies are located according to the underlying distribution of background matter. Morphological types are ascribed according to the morphology-density relation [3]. Galaxies are modeled as nonsingular isothermal spheres, with rotation velocities and core radii that vary with luminosity and morphological types. In Figure 1, we use a series of zooms to illustrate the dynamical range of the density distribution generated by this method.

## 3. THE RAY-TRACING EXPERIMENTS

We consider 3 cosmological models: (1) a flat, cosmological constant model with  $\Omega_0 = 0.27$ ,  $\lambda_0 = 0.73$ , and  $H_0 = 71$  km/s/Mpc. This model is in agreement with the results of the WMAP satellite [2]. (2) a low-density model with  $\Omega_0 = 0.3$ ,  $\lambda_0 = 0$ , and  $H_0 = 75$  km/s/Mpc. (3) a matter-dominated model with  $\Omega_0 = 1$ ,  $\lambda_0 = 0$ , and  $H_0 = 75$  km/s/Mpc. For each model, we consider sources at 5 different redshifts:  $z_s = 1, 2, 3, 4$ , and 5. For each combination model-redshift, we performed 10–20 ray tracing experiments. Each experiment consists of propagating a square beam of  $101 \times 101 = 10,201$  rays back in time from the present to redshift  $z_s$ , through the matter distribution. The rays in the beam were widely separated, by 6 arc minutes, and therefore sampled different regions of space. We computed the magnification matrix  $\mathbf{A}$  along each ray. The magnification  $\mu$  is then

<sup>1</sup>In practice, we combine cubes from different simulations in order to avoid periodicities along the line of sight.

given by

$$\mu = \frac{1}{\det \mathbf{A}}. \quad (1)$$

Figure 2 shows the distribution of magnifications for the  $\Lambda$ -model. The distribution peaks at  $\mu < 1$ , and is strongly skewed. The width of the distribution increases with the source redshift. The distributions for the other two models are qualitatively similar.

#### 4. THE EFFECT OF LENSING ON STATISTICS OF HIGH-Z SUPERNOVAE

Estimating the effect of lensing on the statistics of high- $z$  supernovae is a complex problem, and we defer such analysis to future work. Here we use a simple approach. First, for each model and each source redshift, we compute the standard deviation  $\sigma_\mu$  of the magnification distribution  $P(\mu)$ . The values are shown in Figure 3. We use an empirical fit of the form

$$\sigma_\mu = \frac{az}{1+bz}. \quad (2)$$

This enables us to estimate the values of  $\sigma_\mu$  at any redshift.

We estimate the effect of lensing as follows: the distances of high- $z$  supernovae are reported in the literature as:

$$\log(d_L H_0) = a \pm \delta_a, \quad (3)$$

where  $d_L$  is the luminosity distance,  $H_0$  is the Hubble constant,  $a$  is the measurement, and  $\delta_a$  is the intrinsic uncertainty (i.e. not caused by lensing). The distance  $d_L$  is related to the luminosity  $L$  and flux  $F$  by

$$F = \frac{L}{4\pi d_L^2}. \quad (4)$$

After eliminating  $d_L$ , we get

$$(L/4\pi)^{1/2} H_0 = 10^{a \pm \delta_a} F^{1/2}. \quad (5)$$

The effect of lensing will be to modify the flux  $F$ . To account for it, we replace  $F$  by  $F \pm \Delta F$  in equation (5), and expand to first order in  $\delta_a$  and  $\Delta F$ . After some algebra, we get

$$\log(d_L H_0) = a \pm \delta_a \pm \frac{\Delta F}{2F \ln 10}. \quad (6)$$

The last term represents the effect of lensing. We then make the approximation  $\Delta F/F \approx \sigma_\mu$ , and get

$$\log(d_L H_0) = a \pm \delta_a \pm \delta_\mu, \quad (7)$$

where  $\delta_\mu(z) = \sigma_\mu(z)/2 \ln 10$  is computed using the empirical relations plotted in Figure 3. We use the

values of  $a$  and  $\delta_a$  reported by Tonry et al. [10] (their Table 8). In Figure 4, we plot the ratio  $\delta_\mu/\delta_a$  versus  $z$  (left of the dashed line). This quantity increases with redshift, but never gets higher than 0.5 for the Tonry et al. sample. Furthermore, we shall assume that  $\delta_a$  and  $\delta_\mu$  are statistically independent, and combine them in quadrature, using

$$\delta = (\delta_a^2 + \delta_\mu^2)^{1/2}, \quad (8)$$

where  $\delta$  is the total error. The contribution of lensing to this error is then of order 25% at most.

The top panel of Figure 5 shows a Hubble diagram [deviation  $\Delta(m - M)$  relative to an empty universe, versus redshift], obtained by averaging the data in redshift bins, using

$$w_i = 1/\delta_i^2, \quad (9)$$

$$[\Delta(m - M)]_j = \Sigma_i w_i \Delta(m - M) / \Sigma_i w_i, \quad (10)$$

$$\delta_j = (1/\Sigma_i w_i)^{1/2}, \quad (11)$$

where the sums are over all data points  $i$  in bin  $j$ . The three curves, from top to bottom, show the exact results for the  $\Lambda$ CDM, low-density, and matter-dominated models, respectively. The results support the flat  $\Lambda$ CDM model and exclude the other models considered.

The other panels of Figure 5 show the effect of lensing (the three models have to be plotted separately, because the correction due to lensing is model-dependent). This effect is totally negligible. The largest correction to the error bars is about 10% for the highest redshift bin, for the  $\Lambda$ CDM model.

Clearly, the potential error introduced by lensing is negligible in comparison to the intrinsic error in the measurement, at least for SNe at redshifts  $z < 1.8$ . The next step is to estimate the effect on a yet-undiscovered population of very-high- $z$  SNe. We generated a mock catalog of 43 SNe in the range  $1.8 < z < 8$ . We assume that the values of  $a$  are consistent with a  $\Lambda$ CDM model, and the values of  $\delta_a$  in that range are comparable to the ones in the range  $1.5 < z < 1.8$ .

The ratios  $\delta_\mu/\delta_a$  are plotted in Figure 4. The effect of lensing rapidly becomes important at redshift  $z > 2$ . Figure 6 shows the Hubble diagrams of Figure 5, which have been extended to higher redshifts to include the mock data. The error bars get significantly bigger when lensing is included. Furthermore, at redshift  $z \approx 3$ , it becomes very difficult to distinguish the open, low density model from the cosmological constant model.

#### 5. SUMMARY AND CONCLUSION

We have performed a series of ray-tracing experiments using a multiple lens-plane algorithm. We have estimated the standard deviation of the magnification

distribution with source redshift, for three different cosmological models. Using this relation, we have estimated the effect of lensing on the statistics of high-redshift supernovae. The errors introduced by lensing are unimportant for SNe with redshift  $z < 1.8$ . However, the effect of lensing on a hypothetical population of SNe at redshifts  $z > 1.8$  could be very important, and must be understood before these SNe could be used to constrain cosmological models.

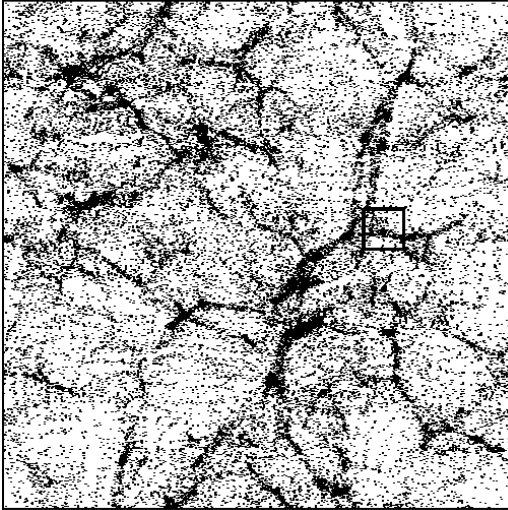
## Acknowledgments

This work benefited from stimulating discussions with Dan Holtz, Christopher Vale, and Karl Gebhardt. HM thanks the Canada Research Chair program and NSERC for support.

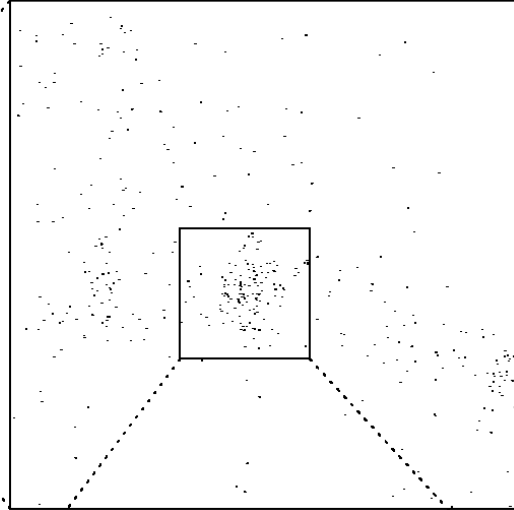
## References

- [1] Barris, B. J. et al. 2004, ApJ, 602, 571
- [2] Bennett, C. L. et al. 2003, ApJS, 148, 1
- [3] Dressler, A. 1980, ApJ, 236, 351
- [4] Martel, H., Premadi, P., & Matzner, R. 1998, ApJ, 497, 512
- [5] Martel, H., Premadi, P., & Matzner, R. 2000, ApJ, 537, 28
- [6] Premadi, P., Martel, H., & Matzner, R. 1998, ApJS, 493, 10
- [7] Premadi, P., Martel, H., Matzner, R., & Futamase, T. 2001a, ApJS, 135, 7
- [8] Premadi, P., Martel, H., Matzner, R., & Futamase, T. 2001b, Pub.A.S.Aus., 18, 201
- [9] Riess, A. G. et al. 2004, ApJ, 607, 665
- [10] Tonry, J. L. et al. 2003, ApJ, 594, 1

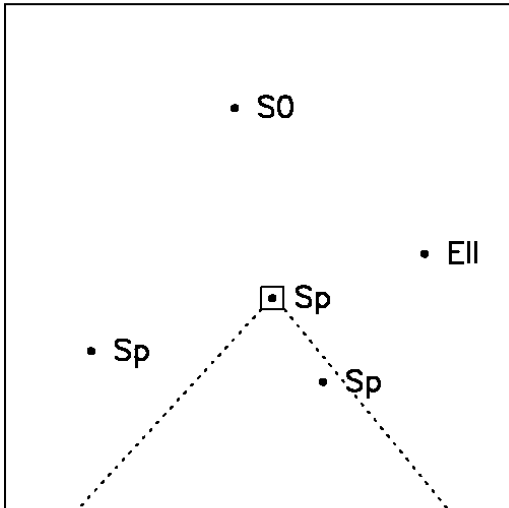
128 Mpc : Superclusters and voids



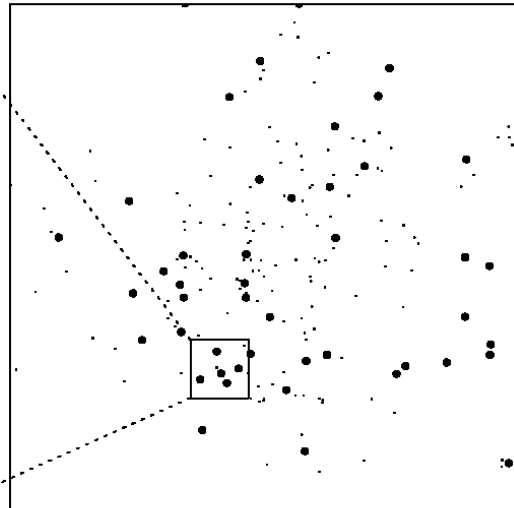
10 Mpc : Clusters of galaxies



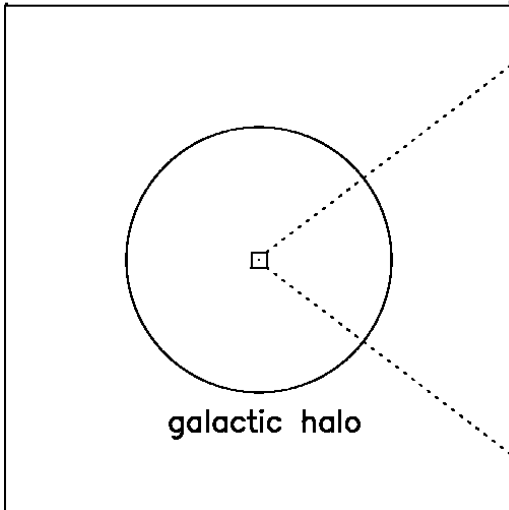
290 kpc : Group of galaxies



2.6 Mpc : Small cluster of galaxies



12.8 kpc : Dwarf spiral galaxy



400 pc : Galactic core

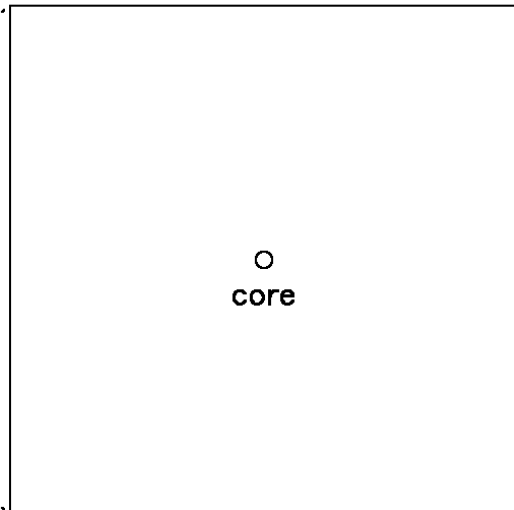


Figure 1: Series of zooms illustrating the dynamical range of the algorithm. Small dots represent P<sup>3</sup>M, dark matter particles. Large dots represent actual galaxies.

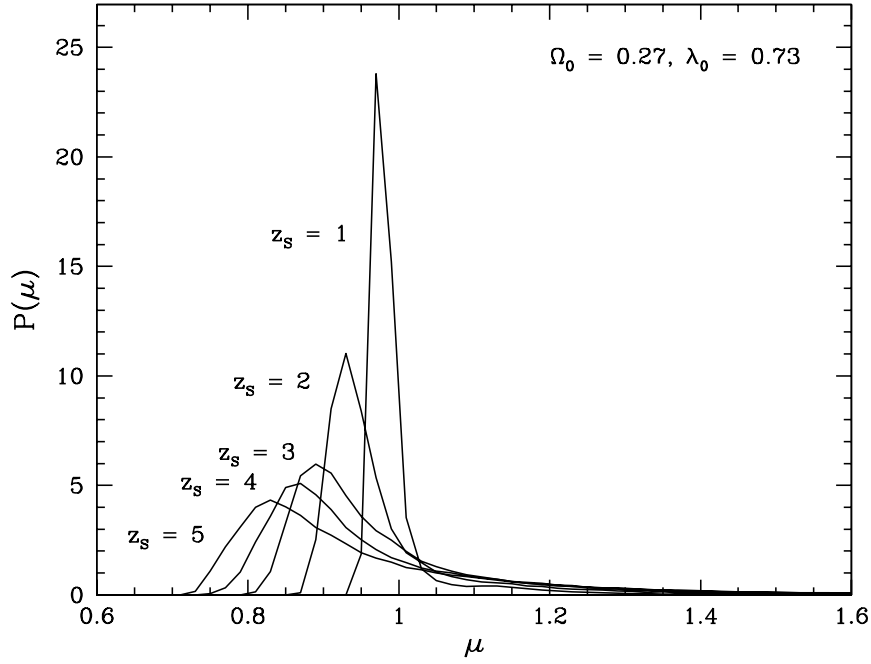


Figure 2: Distribution of magnifications for the  $\Omega_0 = 0.27$ ,  $\lambda_0 = 0.73$  model. The various curves correspond to different source redshifts  $z_s$ , as labelled.

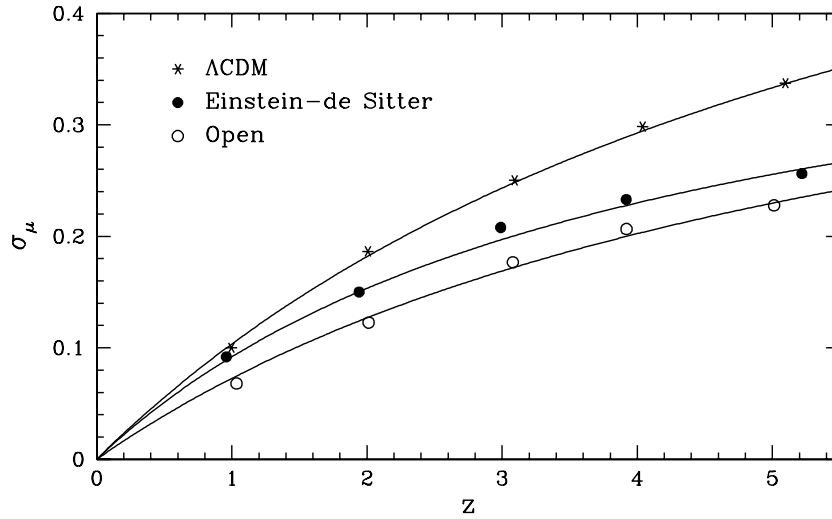


Figure 3: Standard deviation  $\sigma_\mu$  versus redshift, for all three models considered. The solid lines show empirical fits of the form  $\sigma_\mu = az/(1 + bz)$ .

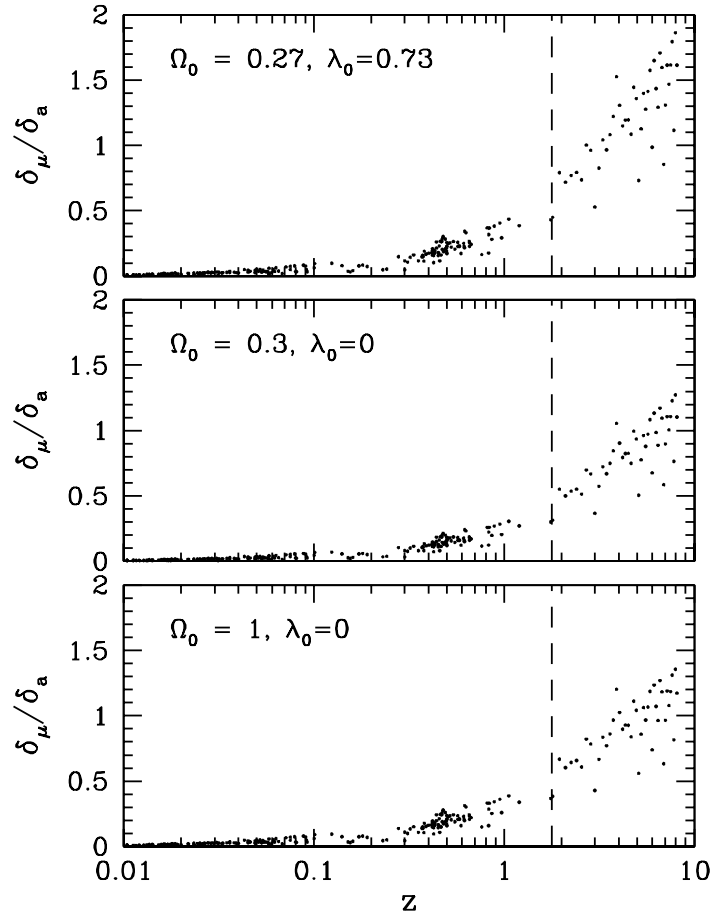


Figure 4: Ratio  $\delta_\mu/\delta_a$  versus redshift. The dashed lines separate the real data of Tonry et al. (left side) from the mock, high-redshift data (right side).

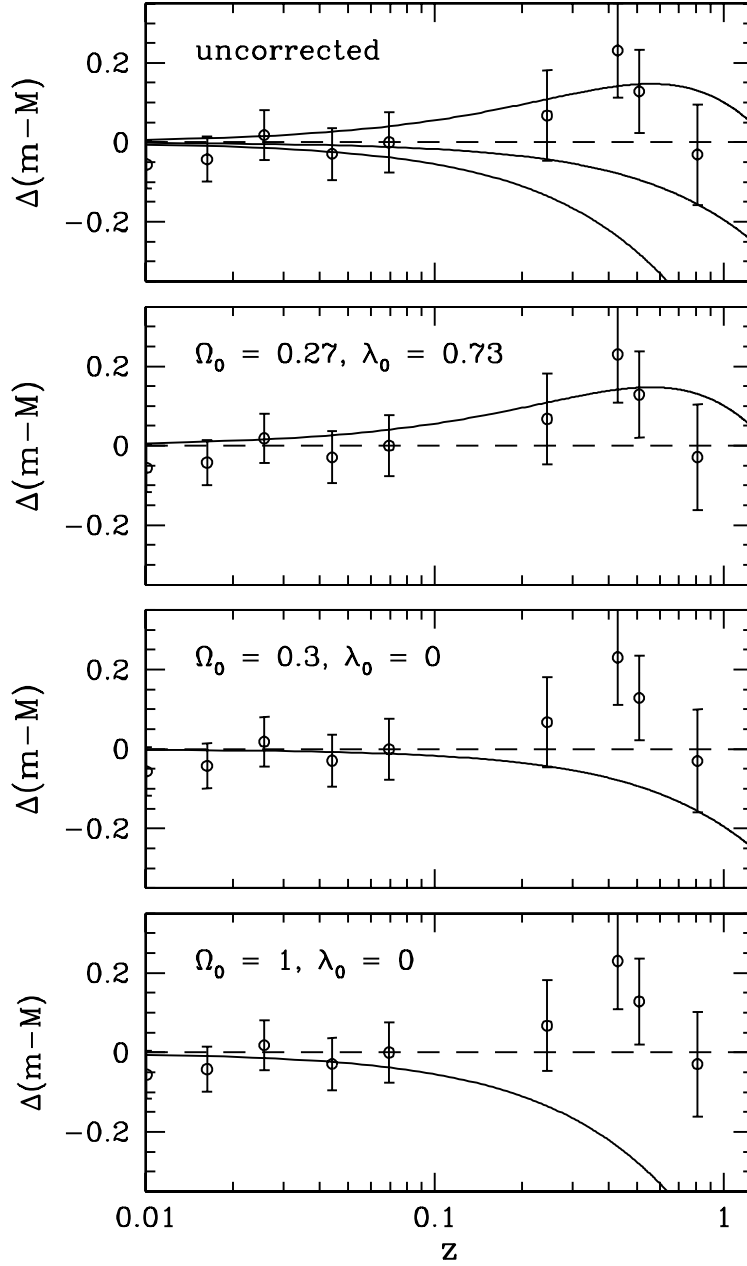


Figure 5: Hubble diagram showing the magnitude deviation  $\Delta(m-M)$  relative to an empty universe, for the three models considered. In the top panel, the three curves, from top to bottom, show the analytical result for the cosmological models  $(\Omega_0, \lambda_0) = (0.27, 0.73)$ ,  $(0.3, 0.0)$ , and  $(1.0, 0.0)$ , respectively. The last three panels reproduce the data of the top panel, but have been corrected to account for lensing. Since this correction is model-dependent, the three models are plotted on separate panels. Error bars show 90% confidence level.

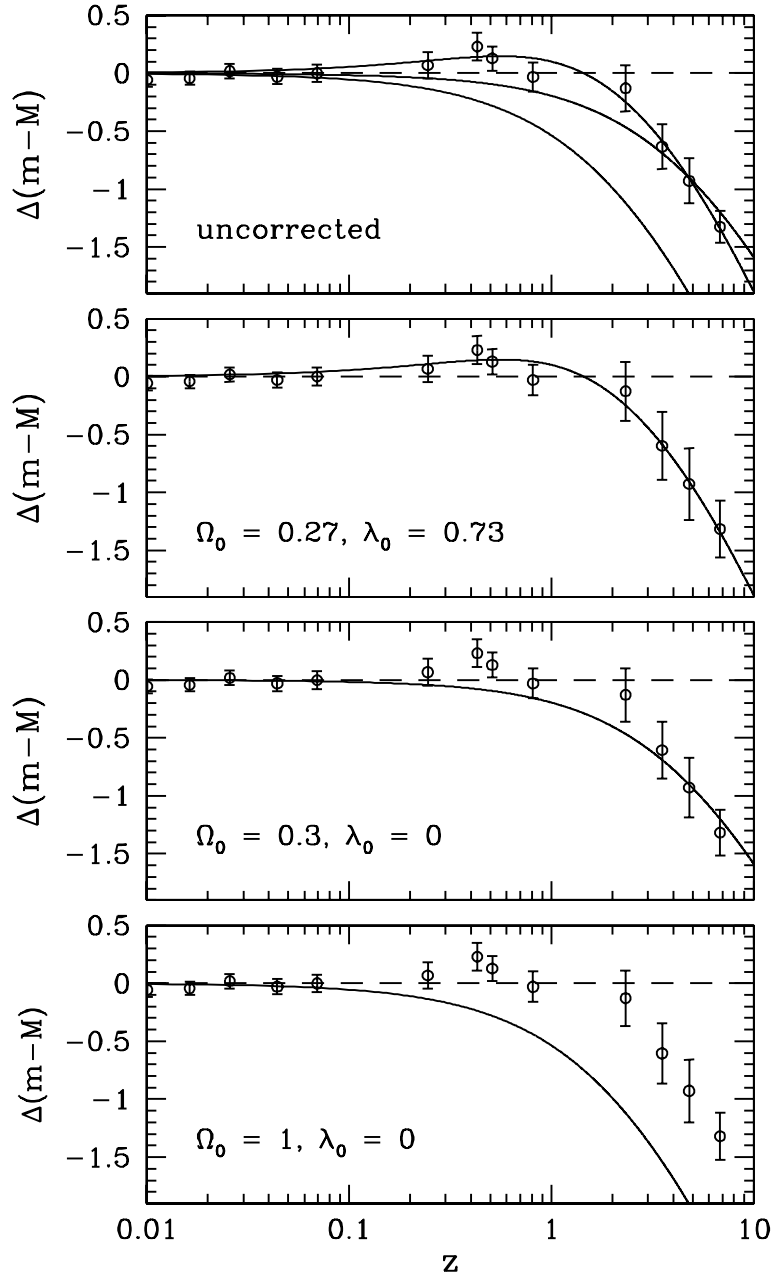


Figure 6: Same as Figure 5, but the panels have been extended to include the mock data (four rightmost data points).